AIAA SciTech Forum
12-16 January 2026, Orlando, FL
AIAA SCITECH 2026 Forum

10.2514/6.2026-2119

Trade Study of Tandem Wing at Hover with Deflected Slipstream Enabled by CoFlow Jet at Low Reynolds number

Jaehyoung Jeon * Anthony Diaz † Yan Ren ‡ Gecheng Zha §
Dept. of Mechanical and Aerospace Engineering
University of Miami, Coral Gables, Florida 33124
E-mail: gzha@miami.edu

Abstract

This paper conducts a trade study of a tandem wing configuration with deflected slipstream enabled by flapped coflow jet (FCFJ) airfoil at hover. The tandem wings are for low Reynolds number condition as a potential application to fly on Mars. The objective is to study the interaction effect of the propellers, the fore and hind wings in order to achieve the required hover lift coefficient with high efficiency. The validated in house FASIP CFD code is used with its unsteady time accurate solver, Spalart-Allmaras (SA) turbulence model, a third-order WENO scheme for inviscid fluxes, and second-order central differencing for viscous terms. The trade study investigates the effects of the streamwise stagger distance (S_t) and transverse vertical gap (G) on aerodynamic performance in 2D and 3D. Results indicate that the 2D configurations with large deflection angles on both the fore airfoil and the hind airfoil exhibit significant wake interference, leading to substantially reduced lift coefficients on the hind airfoil compared to the fore airfoil. When the streamwise distance between the two wings is increased, the interference effect is decreased. To integrate the tandem wings with short streamwise distance, the fore wing is more desirable to generate little slipstream deflection, pull the flow to the hind wing, and keep the flow attached for the hind wing, which will let the hind wing to generate most of the required lift. It is observed that positioning the fore airfoil without deflection and directing its flow toward the hind airfoil achieves high hover lift coefficient and efficiency with reduced propeller power and CFJ momentum coefficients, substantially decreasing the total power consumption.The experience learned from the 2D tandem airfoils configuration for hover is applied to a 3D tandem wing configuration, which has wing span of the fore wing at 1/3 of that of the hind wing. The 3D study also shows that a proper propeller disk load distribution and coflow jet momentum coefficient between the fore and hind wings is crucial to keep the flow attached and achieve the required lift coefficient. The final configuration of this study, which has the disk load of 2.2% pressure rise Dp for the fore wing, 2.7% for the hind wing in the overlapped part, and 4.0% for the outer span of the unoverlapped hind wing, achieves the required lift coefficient with high efficiency. More improvement of the overall efficiency is in progress and will be reported in future. The study indicates that a tandem wing configuration for VTOL aircraft at hover in Martian atmosphere is feasible.

* Ph.D. Candidate
† Master Student
‡ Postdoc Researcher, Ph.D., AIAA member
§ Professor, ASME Fellow, AIAA associate Fellow

Nomenclature

CFJ	CoFlow jet
$FCFJ$	Flapped CoFlow jet
A	Propeller disk area
$AoA(\alpha)$	Angle of attack
LE	Leading Edge
TE	Trailing Edge
C_L	Lift coefficient $L/(q_\infty S)$
C_D	Drag coefficient $D/(q_\infty S)$
C_μ	Jet momentum coef. $\dot{m}_j U_j/(q_\infty S)$
$(C_L/C_D)_c$	CFJ airfoil corrected aerodynamic efficiency $C_L/(C_D$+Pc)
$(C_L^2/C_D)_c$	CFJ airfoil corrected productivity efficiency $C_L^2/(C_D$+Pc)
D	Propeller Diameter
DS	Deflected Slipstream
DL	Disk loading, thrust of actuator disk/actuator disk area
DL_c	Disk loading coefficient
FM_{DS}	Figure of Merit for the DS system
G	Vertical distance between the two airfoils, gap
P_{tot}	Total power of the DS-CFJ system
P_P	Propeller actuator power coefficient $\frac{2}{\rho V_\infty^3 S}\sqrt{\frac{F^3}{2\rho A}}$
PL	Power loading, power/lift
PL_c	Power loading coefficient
ΔP	Pressure percentage increase across the propeller actuator disk
R	Propeller disk radius
R_e	Reynolds number
M	Mach number
S	Planform area of the airfoil
S_t	Longitudinal separation of the two airfoils, stagger
T_t	Total temperature
P_t	Total pressure
H_t	Total specific enthalpy
U	Flow velocity
P	Pumping power
Pc	Power coefficient $P/(q_\infty S V_\infty)$
c_p	Constant pressure specific heat
γ	Air specific heats ratio
s	airfoil Span length
c	Profile chord
q	Dynamic pressure $0.5\,\rho U^2$
p	Static pressure
ρ	Air density
Γ	Total pressure ratio of CFJ pump
β	Deflection angle
ϵ	Resultant force angle
$\dot{m}$	Mass flow across the pump
θ	airfoil tilting angle

∞	Subscript, stands for free stream
j	Subscript, stands for jet

1 Introduction

The increasing interest in Mars exploration has driven a need for technological advancements to extend the operational range of aerial vehicles on the Martian surface. Mars' unique environment presents significant challenges for aerial mobility due to its thin atmosphere and varied terrain. To overcome these obstacles, high-performance, efficient aircraft specifically designed for Mars are essential for future missions. Such aircraft could greatly enhance mobility and accessibility, facilitating the exploration of vast Martian landscapes, enabling resource discovery, identifying potential water and ice deposits, detecting methane sources and magnetic field, and providing insights into Martian geological history.

Vertical takeoff and landing (VTOL) fixed wing aircraft is appealing for missions on Mars due to its high efficiency and unique capability for runway-independent operations. Recently, Zha et al [1] have developed a solar powered fixed wing VTOL aircraft concept MAGGIE (Mars Aerial and Ground Global Intelligent Explorer), which is energy self-sufficient and has a global scale range in one Martian year to survey the entire Martian surface and atmosphere. MAGGIE utilizes a tandem wing (Canard) configuration, which can potentially achieve a very high cruise lift coefficient of $C_L = 3.24$ and the corrected aerodynamic efficiency of 5.76 enabled by CoFlow Jet (CFJ) active flow control [2]. The design adopts a vortex capturing technique developed by Ren and Zha [3].

MAGGIE utilizes an advanced deflected slipstream technology for VTOL hover-cruise transition without using tiltrotors, tiltwings, and lift-plus-configurations [1, 4, 5, 6]. The propellers will be always fixed at the forward-facing direction for cruise. The hover lift is generated by a CoFLow Jet flap that deflects the slipstream from the propellers vertically downward. Ren and Zha [7] simulate the single 2D airfoil is the hover-cruise transition with automatic control of the fluid-body interaction. However, the tandem wings interaction with deflected slipstream at hover for both 2D and 3D flows is not well understood.

The purpose of this paper is to investigate the interaction effect of a tandem wings configuration at hover enabled by deflected slipstream, which is achieved by CFJ at low Reynold number to mimic Martian atmospheric conditions . Understanding this effect is crucial to achieve high efficiency design of of the hover maneuver of VTOL aircraft enabled by deflected slipstream.

1.1 Flapped CoFlow Jet airfoil

The flapped coflow jet airfoil is adopted to achieve deflected slipstream for VTOL aircraft [5, 6, 1]. The CFJ is applied inside a long flap that is a part of the flapped CFJ airfoil, as shown in Fig.1 [8], which has the injection located at the shoulder of the flap, the suction slot is located near trailing edge. A micro-compressor actuator is embedded inside the airfoil as the pumping system, which pressurizes the mass flow withdrawn from the suction slot and then ejects at the injection slot. By deflecting the flap rather than rotating the front of the airfoil, the FCFJ airfoil has the advantage of allowing the airfoil to change the angle of attack and lift coefficient without tilting the airfoils or the aircraft.

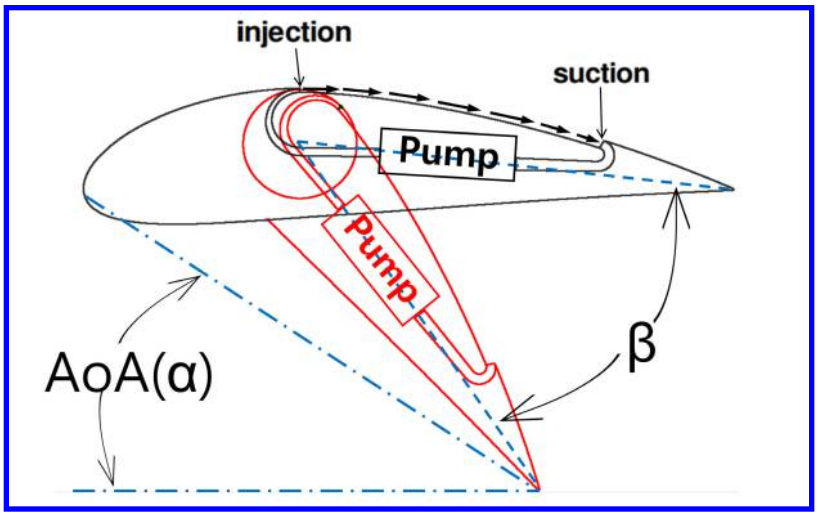

Figure 1: Sketch of flapped CFJ airfoil with the CoFlow jet applied on the flap

2 The Tandem airfoil configuration

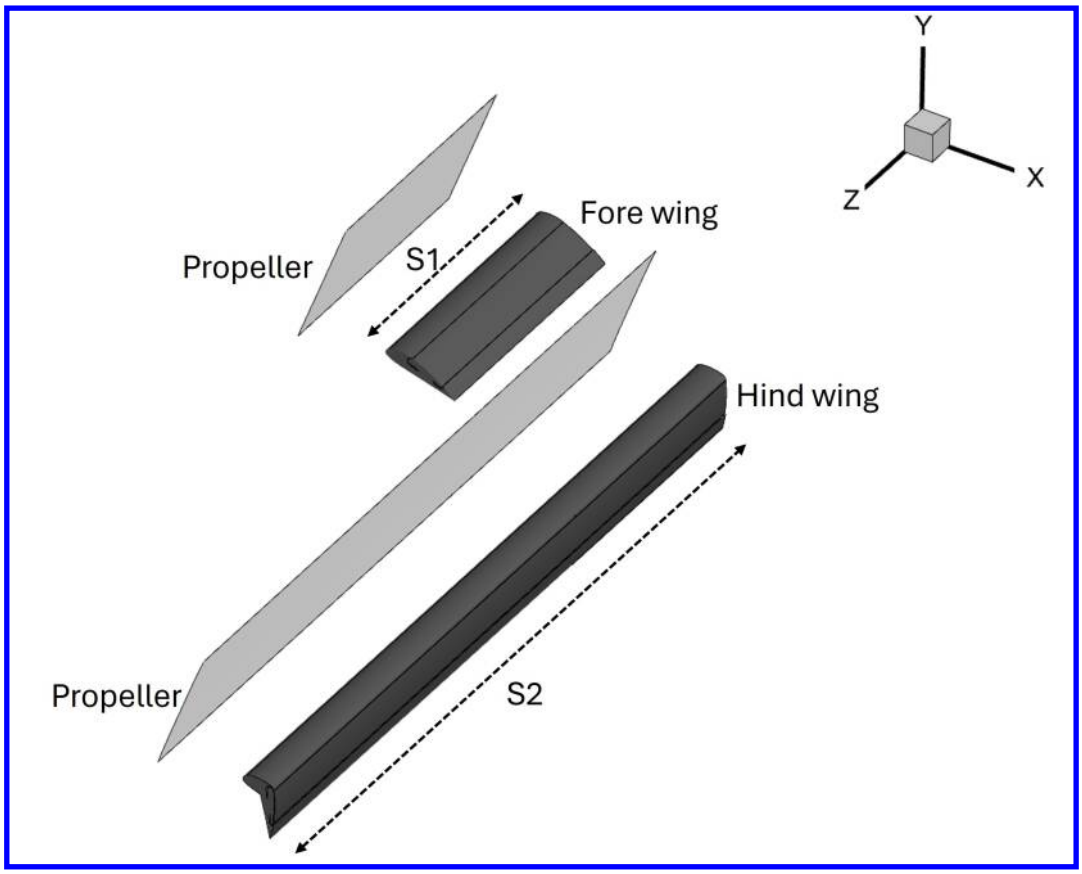

Figure 2: 3D view of the tandem wing configuration

The 3D tandem wing system is shown in Fig. 4. A cross section of the overlapped part of the fore wing and hind wing is shown in Fig. 4. The system consists of a fore airfoil and hind airfoil arrangement with vertically mounted propellers. The entire assembly is tilted by an angle θ from the horizontal plane to mitigate the hover power. Each wing is implemented with coflow jet (CFJ) in the flap. The epsilon angle(ϵ) stands for the resultant force direction about the horizontal direction. If epsilon is 90deg, the resultant force is fully vertical. If the angle $\epsilon = atan(C_D/C_L) > 0$, the resultant force has a drag component pointing downstream (right), otherwise, if $\epsilon < 0$, it has a thrust component pointing upstream.

As illustrated in Fig. 3, the key geometric parameters defining the tandem airfoil configuration are the longitudinal separation, denoted as stagger (S_t), which represents the streamwise distance between the fore and hind wing leading edge positions, and the vertical gap (G), which defines the vertical separation between the airfoil mean aerodynamic center lines. The flap deflection angle β serves as a critical control parameter that controls the flow turning angle of the deflected slipstream pulled from the propellers.

This paper conducts trade study of the stagger and gap in 2D first, and then apply the configuration to 3D to optimize the system.

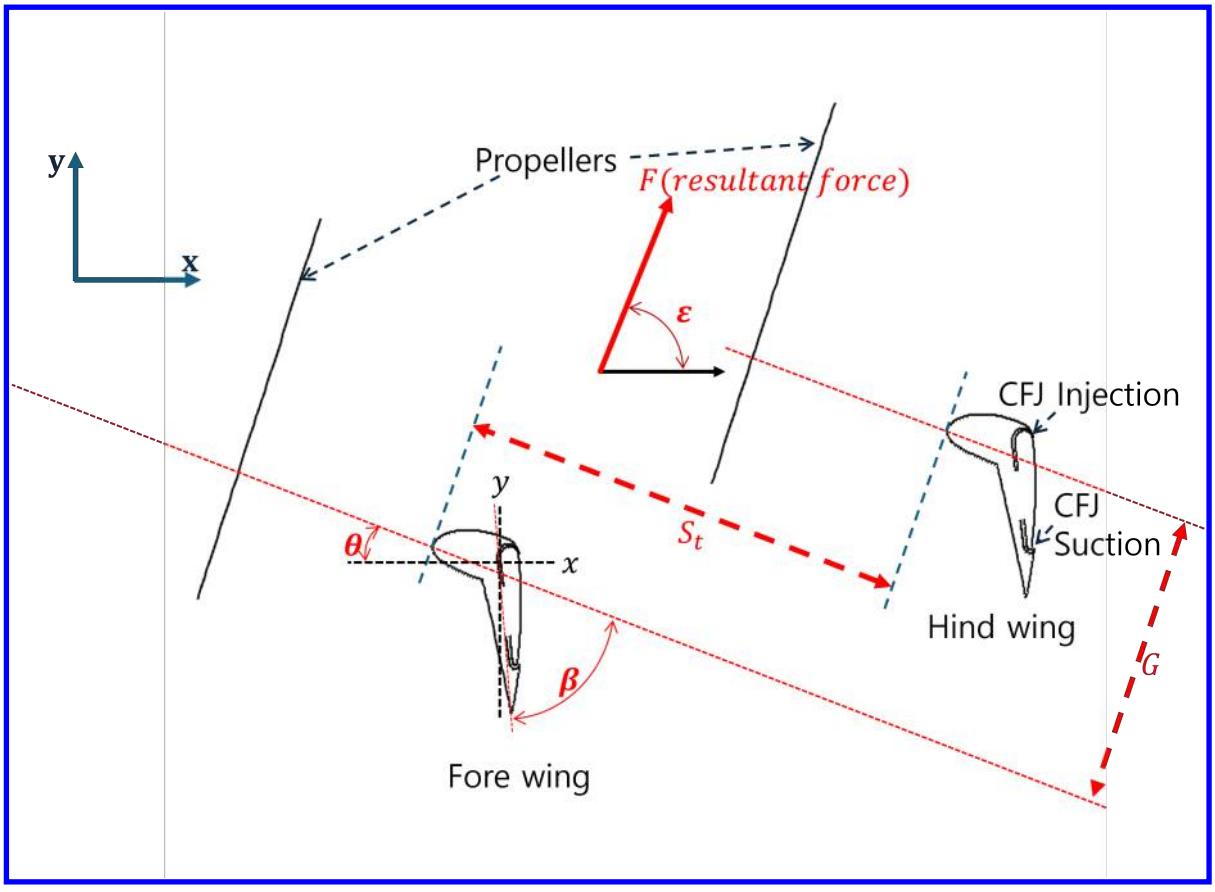

Figure 3: Schematic of Tandem airfoil configuration

3 Methodology

3.1 Lift and Drag Calculation

The momentum and pressure at the injection and suction slots produce a reactionary force, which is automatically measured by the force balance in wind tunnel testing. However, for CFD simulation, the full reactionary force needs to be included. Using control volume analysis, the reactionary force can be calculated using the flow parameters at the injection and suction slot opening surfaces. Zha et al. [9] give the following formulations to calculate the lift and drag due to the jet reactionary force for a CFJ airfoil. By considering the effects of injection and suction jets on the CFJ airfoil, the expressions for these reactionary forces are given as :

$$F_{x_{cfj}} = (\dot{m}_j V_{j1} + p_{j1} A_{j1}) * cos(\theta_1 - \alpha) - (\dot{m}_j V_{j2} + p_{j2} A_{j2}) * cos(\theta_2 + \alpha) \tag{1}$$

$$F_{y_{cfj}} = (\dot{m}_{j1} V_{j1} + p_{j1} A_{j1}) * sin(\theta_1 - \alpha) + (\dot{m}_{j2} V_{j2} + p_{j2} A_{j2}) * sin(\theta_2 + \alpha) \tag{2}$$

where the subscripts 1 and 2 stand for the injection and suction respectively, and θ_1 and θ_2 are the angles between the injection and suction slot's surface and a line normal to the airfoil chord. α is the angle of attack.

The total lift and drag on the airfoil can then be expressed as:

$$D = R'_x - F_{x_{cfj}} \tag{3}$$

$$L = R'_y - F_{y_{cfj}} \tag{4}$$

where R'_x and R'_y are the surface integral of pressure and shear stress in x (drag) and y (lift) direction excluding the internal ducts of injection and suction. For CFJ airfoil simulations, the total lift and drag are calculated by integrating Eqs.(3) and (4) in the spanwise direction.

3.2 Jet Momentum Coefficient

The jet momentum coefficient C_μ is a parameter used to quantify the jet intensity. It is defined as:

$$C_\mu = \frac{\dot{m} V_j}{\frac{1}{2} \rho_\infty {V_\infty}^2 S} \tag{5}$$

where $\dot{m}$ is the injection mass flow, V_j is the mass-averaged injection velocity, ρ_∞ and V_∞ denote the free stream density and velocity, and S is the planform area.

3.3 Micro-compressor Power Coefficient

CFJ is implemented by mounting a pumping system inside the airfoil that withdraws air from the suction slot and blows it into the injection slot. The power consumption is determined by the jet mass flow and total enthalpy change as the following:

$$P = \dot{m}(H_{t1} - H_{t2}) \tag{6}$$

where H_{t1} and H_{t2} are the mass-averaged total enthalpy in the injection cavity and suction cavity respectively, P is the Power required by the pump and $\dot{m}$ the jet mass flow rate. Introducing P_{t1} and P_{t2} the mass-averaged total pressure in the injection and suction cavity respectively, the compressor efficiency η, and the total pressure ratio of the pump $\Gamma = \frac{P_{t1}}{P_{t2}}$, the power consumption is expressed as:

$$P = \frac{\dot{m} C_p T_{t2}}{\eta}(\Gamma^{\frac{\gamma-1}{\gamma}} - 1) \tag{7}$$

where γ is the specific heat ratio equal to 1.4 for air. The power coefficient is expressed as:

$$P_c = \frac{P}{\frac{1}{2}\rho_\infty V_\infty^3 S} \tag{8}$$

3.4 Aerodynamic Efficiency

The conventional airfoil aerodynamic efficiency is defined as:

$$\frac{C_L}{C_D} \tag{9}$$

For the CFJ airfoil, the ratio above still represents the pure aerodynamic relationship between lift coefficient and drag coefficient. However since CFJ active flow control consumes energy, the ratio above is modified to take into account the energy consumption of the micro-compressor. The formulation of the corrected aerodynamic efficiency for CFJ airfoils is:

$$(\frac{C_L}{C_D})_c = \frac{C_L}{C_D + P_c} \tag{10}$$

where P_c is the micro-compressor power coefficient defined in Eqn. 8 and C_L and C_D are the lift and drag coefficients of the CFJ airfoil. If the micro-compressor power coefficient is set to 0, this formulation returns to the aerodynamic efficiency of a conventional airfoil.

This study involves a tandem airfoil configuration. For example, the coefficient of lift and drag for each wing are defined individually as:

$$C_{L1} = \frac{L_1}{\frac{1}{2}\rho_\infty V_\infty^2 S_1}, \quad C_{L2} = \frac{L_2}{\frac{1}{2}\rho_\infty V_\infty^2 S_2}, \tag{11}$$

$$C_{D1} = \frac{D_1}{\frac{1}{2}\rho_\infty V_\infty^2 S_1}, \quad C_{D2} = \frac{D_2}{\frac{1}{2}\rho_\infty V_\infty^2 S_2}, \tag{12}$$

where the subscript 1 and 2 stand for the first and second airfoil. For the aircraft system with tandem airfoils, the system lift coefficient is defined as the total lift based on the total airfoil area below:

$$C_{Lt} = \frac{L_1 + L_2}{\frac{1}{2}\rho_\infty V_\infty^2 (S_1 + S_2)} \tag{13}$$

where the subscript t stands for tandem airfoil.

Substituting Eq. (11) to Eq. (13), the system lift coefficient can be expressed as:

$$C_{Lt} = \frac{C_{L1} S_1 + C_{L2} S_2}{S_1 + S_2} \tag{14}$$

Eq. (14) is actually the same as the area weighted lift coefficient. Similarly, the coefficient of system drag and CFJ power can be defined as:

$$C_{Dt} = \frac{C_{D1} S_1 + C_{D2} S_2}{S_1 + S_2} \tag{15}$$

$$P_{ct} = \frac{P_1 S_1 + P_2 S_2}{S_1 + S_2} \tag{16}$$

The corrected drag coefficient is:

$$(C_{Do})_t = C_{Dt} + P_{ct} \tag{17}$$

The aerodynamic efficiency and the productivity efficiency of the tandem airfoil system then can be defined following the same way as Eq. (5) and Eq. (10). To see the relations clearly, we take the aerodynamic efficiency of the tandem airfoil as an example below:

$$\begin{aligned}\left(\frac{L}{D}\right)_t &= \frac{L_1 + L_2}{D_1 + D_2 + P_1/V_\infty + P_2/V_\infty} = \frac{C_{Lt}\frac{1}{2}\rho_\infty V_\infty^2 (S_1 + S_2)}{C_{Dt}\frac{1}{2}\rho_\infty V_\infty^2 (S_1 + S_2) + P_{ct}\frac{1}{2}\rho_\infty V_\infty^2 (S_1 + S_2)} \\ &= \frac{S_1 C_{L1} + S_2 C_{L2}}{S_1 C_{D1} + S_2 C_{D2} + S_1 P_{ct} + S_2 P_{ct}}\end{aligned} \tag{18}$$

That is:

$$\left(\frac{L}{D}\right)_t = \frac{C_{Lt}}{(C_{Do})_t} \tag{19}$$

3.5 Disk Loading and Power Loading

For rotorcraft aerodynamics, the ideal power coefficient for the propeller-based actuator disk momentum theory at static condition is:

$$P_p = \frac{2}{\rho_\infty V_\infty^3 S}\sqrt{\frac{L^3}{2\rho A}} \tag{20}$$

where A is the actuator disk area; L is the total force produced by the propeller actuator normal to the propeller disk. L would be the lift for a vertical rotor or thrust for a horizontal rotor. The same reference parameters for the airframe aerodynamic parameters are used to normalize the rotor parameters to be consistent.

Disk loading and power loading are used to describe rotorcraft VTOL performance. The disk loading (DL) is defined as

$$DL = \frac{L}{A} \tag{21}$$

The disk loading is closely related to the noise produced by a rotor. A higher disk loading will in general generate louder noise. The power loading (PL) for a propeller disk at static hovering condition is defined as

$$PL = \frac{P}{L} \tag{22}$$

where P is the propeller power used to generate the lift L. The power loading indicates the power required per unit lift for rotorcraft. The disk loading and power loading coefficients are defined as follows:

$$DL_c = \frac{DL}{0.5\rho_\infty V_\infty^2} = \frac{C_L}{A_c} \tag{23}$$

where $C_L = L/(0.5\rho V^2 S)$, $A_c = A/S$, A is the disk area and S is the airfoil planform area.

$$PL_c = \frac{PL}{V_\infty} = \frac{P_p}{C_L} \tag{24}$$

The actuator DL and PL have the following relations in hover static condition:

$$PL = \sqrt{\frac{DL}{2\rho}} \tag{25}$$

$$PL_c = \frac{\sqrt{DL_c}}{2} \tag{26}$$

3.6 Figure of Merit for DS-CFJ Hover

To compare the efficiency of the DS-CFJ hover system with a vertical rotor with the same total lift and disk size, we adopt a parameter FM_{DS} similar to the figure of merit (FM) of rotorcraft below:

$$FM_{DS} = \frac{P_p}{P_{DS-CFJ}} = \frac{P_p}{P_{prop} + P_c} \tag{27}$$

$$P_{total} = P_{DS-CFJ} = P_{prop} + P_c \tag{28}$$

where P_p is the ideal power coefficient required by a vertical rotor disk that generates the same lift of the DS-CFJ system with the same rotor disk size based on Eq. 20. The total power required by the DS-CFJ system P_{DS-CFJ} is the summation of the propeller power P_{prop} and the CFJ power P_c.

To isolate the CFJ effect in the parameter FM_{DS}, the propeller power P_{prop} of the DS-CFJ system is also calculated based on the disk theory formulation Eq. 20, which uses the disk loading determined by the pressure rise imposed on the disk as the boundary condition. The CFJ power required P_c is determined by Eq. 7 and 8. The power coefficient P_c studied in this paper includes all the viscous effect of the DS-CFJ system governed by Reynolds averaged Navier-Stokes (RANS) equations, but the CFJ actuator efficiency in Eq. 7 is set to be 100% to consider only the power required to achieve the AFC performance. Currently, the efficiency of a micro-compressor with the diameter of 64 mm we have designed is slightly more than 84% [10]. In an integrated system with a CFJ airfoil and a micro-compressor actuator, the micro-compressor efficiency is designed to 76%-80% [11, 12]. Such efficiency corresponds to a typical figure of merit of vertical rotors. With more design optimization, a higher micro-compressor efficiency is achievable. If FM_{DS} is equal to one, the DS-CFJ system has the same hover efficiency as a vertical rotor with the same rotor disk size.

3.7 CFD Simulation Setup

The FASIP(Flow-Acoustics-Structure Interaction Package) CFD code is used to conduct the numerical simulation. The 2D unsteady Reynolds Averaged Navier-Stokes (URANS) equations with one-equation Spalart-Allmaras(SA) turbulence model is used. A 3rd order WENO scheme for the inviscid flux [13, 14, 15, 16, 17, 18] and a 2nd order central differencing for the viscous terms [13, 17] are employed to discretize the Navier-Stokes equations. The low diffusion E-CUSP scheme used as the approximate Riemann solver suggested by Zha et al [14] is utilized with the WENO scheme to evaluate the inviscid fluxes. Implicit time marching method using Gauss-Seidel line relaxation is used to achieve a fast convergence rate [19]. Parallel computing is implemented to save wall clock simulation time [20].

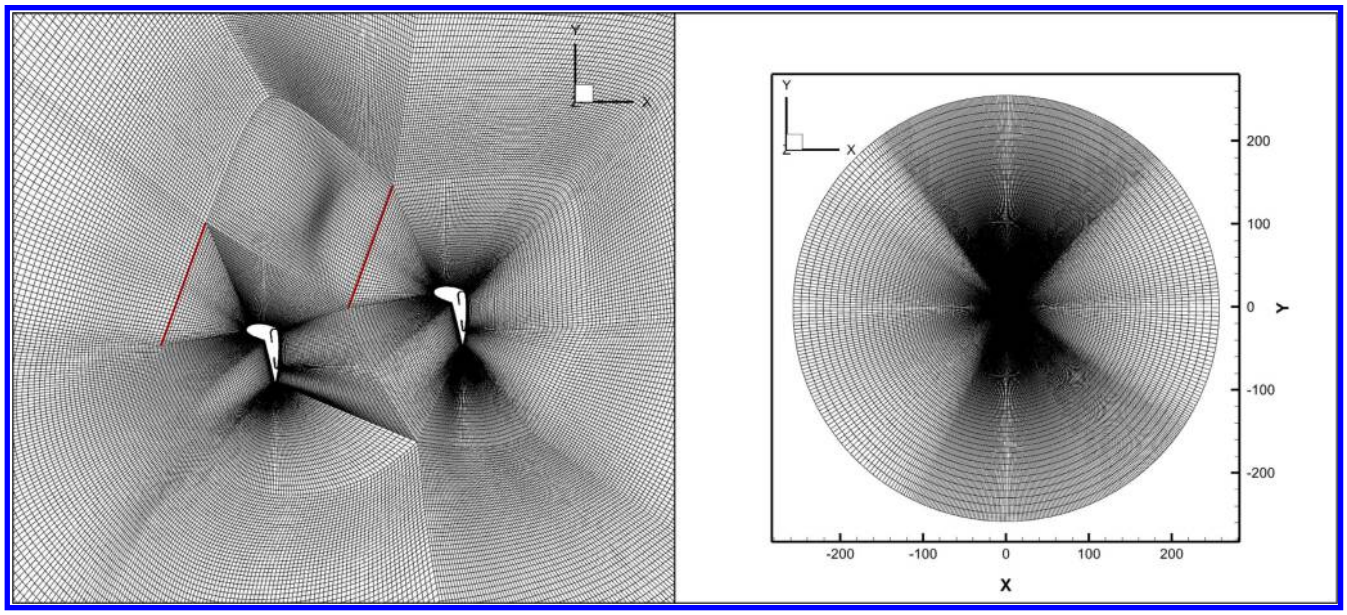

Figure 4: 2D mesh for tandem airfoil configuration of the hover condition.

3.8 Boundary Conditions

The 3rd order accuracy no slip condition is enforced on the solid surface with the wall treatment suggested in [21] to achieve the flux conservation on the wall. The far field boundary is located at 500 chord with a O-mesh topology. The far filed is at static condition with velocity set to be zero. The large farfield domain is to facilitate a solid convergence of computing the flows at static conditions that is largely incompressible, which may make a Navier-Stokes solver for compressible flows more stiff. The computational mesh is shown in Fig. 4. Total pressure, total temperature and flow angles are specified at the injection duct inlet, as well as the upstream portion of the far field. For the static condition, the static pressure at the downstream farfield is set to be equal to the total pressure at upstream far field. Constant static pressure is applied at the suction duct outlet as well as the downstream portion of the far field. The actuator disk BC is modeled as a flat surface, across which the static pressure is increased by a percentage Δp based on the local static pressure upstream of the disk. Even though the pressure increase percentage is uniform across the disk, the pressure increase is not due to the non-uniform local static pressure upstream of the disk. The pressure jump across the disk is handled by the approximate Riemann solver in the FASIP code similar to a shock wave.

To avoid being divided by 0, the freestream reference condition at Mach number of 0.04 is chosen to be used to normalize the aerodynamic parameters at static conditions. They include $V_\infty = 9.3\,\mathrm{m/s}$ and $\rho_\infty = 0.0158\,\mathrm{kg/m^3}$. The first grid point on the airfoil surface is placed at $y^+ \approx 1$.

The atmospheric properties for Mars, relevant to the present analysis, are summarized in Table 1.

Table 1: Flow Conditions and Properties

Variable	**Value**	**Unit**
p	655	[Pa]
T	220	[K]
ρ	0.01576	[kg/m^3]
μ	1.11E-05	[kg/m s]
R	188.9	[J/kg K]
L_{ref}	1	[m]
U_∞	9.3	[m/s]
γ	1.3	
M_∞	0.04	
Re_∞	1.32E+04	

4 2D Results

Previous single airfoil research [22] demonstrated that by tilting up the airfoil with a small angle, the system could achieve the required lift through combined contributions of CFJ flow turning and propeller-generated lift force, rather than relying solely on CFJ for flow deflection. This is particular useful at low Reynolds number condition that the overall system efficiency is reduced. Building upon these findings, the present study investigates a configuration with a total tilting angle θ of 20 degrees. As illustrated in Fig. 5, when both fore airfoil and hind airfoil operate with large deflection angles, significant flow interaction between the airfoils becomes evident. The results presented in Table 2 reveal that for Case 1 and Case 2, with stagger distances S_t of 5C and 10C respectively, the hind airfoil exhibits substantially lower lift coefficients compared to the fore airfoil. Even in Case 2 with $S_t = 10C$, while the fore airfoil achieves a lift coefficient exceeding 70, the hind airfoil barely reaches half of this value. Considering typical aircraft fuselage dimensions, such a design configuration appears aerodynamically inefficient. The reason appears to be that when the two airfoils are close with St=5C (Fig. 5, left), the front propeller pulls a strong slipstream deflected downward by the fore FCFJ airfoil. It is difficult for the rear propeller to withdraw sufficient flow when the flow upstream is mostly moving downward. The flow around the hind airfoil is not established and thus the lift coefficient is very low as shown in Table 2. When the St is increased to 10C (Fig. 5, right), the lift coefficient of the hind airfoil is substantially increased by 140% since there is abundant flow to be pulled to the rear propeller. This is simply because when the two airfoils are far apart, the interference is much weaker. However, a St of 10C may not be always available depending on the aircraft size. The Table 2 presents results where individual components (fore airfoil, hind airfoil, and propeller) are normalized using a 1 chord length reference. The parameter calculation of the individual wing and the tandem wing system is based on Eq. (14) -(21). The total power is based on Eq. (28).

Table 2: Results for Fig. 5

Case	Part	S_t	G	β	Δp (%)	C_μ	C_L	C_D	P_c	Γ	ϵ
Case 1	Fore airfoil	5C	0.35C	60	4.5	10	66.73	91.56	164.2	2.30	
	Hind airfoil			60	4.5	10	15.56	13.87	170.8	2.35	
	Propeller						25.54	-70.19	172.5		
	Total						66.69	-17.47	340.0		104.7
Case 2	Fore airfoil	10C	0.35C	60	4.5	10	70.02	72.55	170.14	2.41	
	Hind airfoil			60	4.5	10	37.27	52.78	147.33	2.13	
	Propeller						25.21	-69.27	169.15		
	Total						78.86	-6.60	327.9		94.8

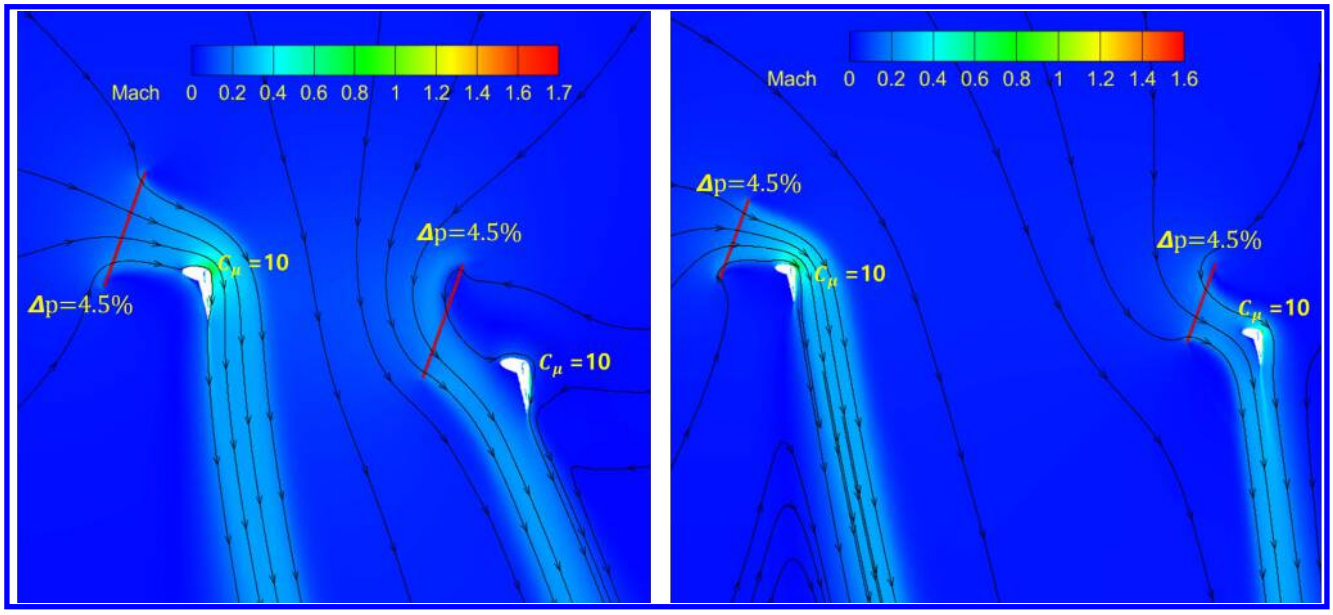

Figure 5: Flow Field :Case 1 : S_t=5, G=0.35 (left) ;Case 2: S_t=10, G=0.35 (right)

Clearly, the challenge is how to make a tandem wing system work efficiently without requiring a large distance between the two wings. As depicted in Fig. 6, one way is to let the fore airfoil has no deflection and direct all flow toward the hind airfoil. This would favor the hind airfoil in particular if the hind wing is the main wing with a longer wingspan. In this configuration, the fore airfoil pulls more flow to the hind airfoil with increased dynamic pressure. The rear wing can deflect the flow very well downward with reduced CFJ power. When compared to the single airfoil with $\Delta p = 4.5\%$ and C_μ of 5, both the CFJ power and total system power are substantially reduced by 67% [22]. As shown in Fig 6, with the undeflected fore airfoil, the flow is well attached for the hind airfoil. Compare the Case 3 in Table 3 with the Case 2 in Table 2, the hind airfoil has about the same C_L, but its power coefficient is reduced by 66%. The analysis results shown in Table 3 demonstrate that this configuration can achieve the target lift coefficient for hover flight using a relatively low propeller disk loading ($\Delta p = 2\%$) and reduced CFJ momentum coefficient (C_μ), indicating a more efficient operational strategy.

Table 3: Results for Fig. 6

Case	Part	S_t	G	β	Δp (%)	C_μ	C_L	C_D	P_c	Γ	ϵ
Case 3	Fore airfoil	2.5C	0	0	2.0	1	7.53	3.93	6.46	1.12	
	Hind airfoil			60	2.0	5	37.09	53.25	50.32	1.53	
	Propeller						12.5	-34.35	59.08		
	Total						34.81	-5.77	87.46		99.4
Case 4	Fore airfoil	2.5C	0.5C	0	2.0	1	7.62	3.91	6.47	1.12	
	Hind airfoil			60	2.0	5	32.72	39.83	56.94	1.53	
	Propeller						12.32	-33.86	57.80		
	Total						32.49	-11.99	89.51		110.3
Case 5	Fore airfoil	2.5C	-0.5C	0	2.0	1	3.70	2.51	6.52	1.13	
	Hind airfoil			60	2.0	5	40.21	56.48	50.47	1.55	
	Propeller						13.13	-36.07	63.56		
	Total						35.08	-6.58	92.05		100.6

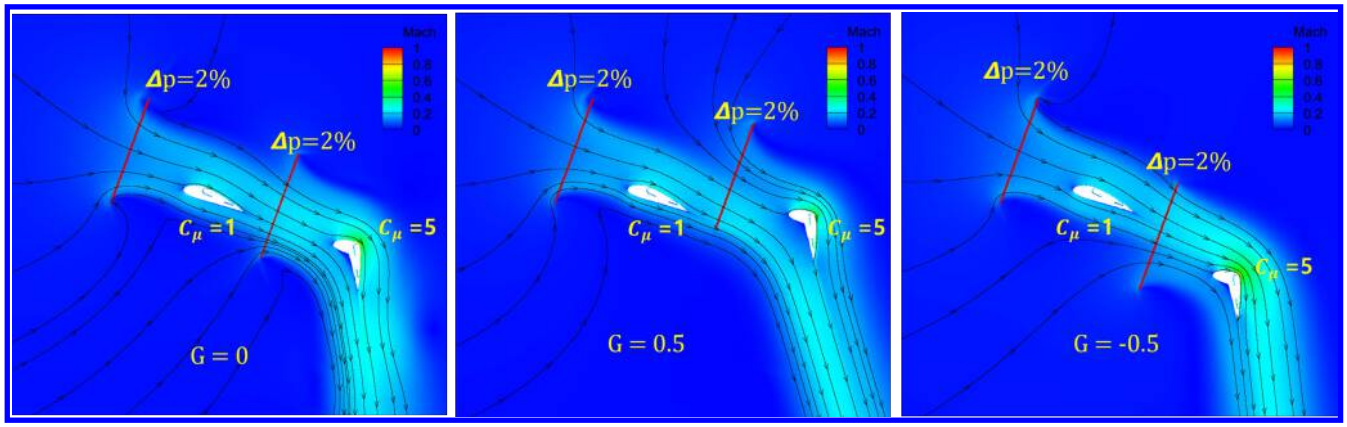

Figure 6: Flow Field (Case 1 : G=0.0 (left), Case 2: G=0.5 (middle), Case 3: G=-0.5 (right)

5 3D Results

The experience learned from the 2D will be applied to the 3D tandem configuration shown in Fig. 4, which has the aspect ratio of 6.66 and 20 respectively for the fore wing and hind wing. However, 3D configuration is actually very different from the 2D. Each wing will have its wing tip vortex. The two wings also do not have the same wing span.

The propeller configuration utilizes a diameter of 1.75C positioned 1.0C upstream of the leading edges of both wings, with approximately 65% of the propeller disk located above the wing leading edge. This arrangement enables effective slipstream deflection through the combined action of both wings. As shown in Fig. 4, the propellers of each wing are simulated as a rectangle disk to mimic a series of round propeller disks aligned next to each other. The computational mesh (Fig. 7) consists of approximately 27.5 million cells distributed across 225 computational blocks to ensure adequate resolution of the complex three-dimensional flow phenomena. The mesh has hind wing span of 10C and the fore wing span of

approximately one-third the hind wing span (3.33C). This span ratio reflects the design philosophy where the fore wing serves as a control surface and will pull flow toward the hind wing, which provides the dominant contribution to total lift generation through its larger planform area and flow deflection capability.

A systematic parametric study was conducted to investigate the influence of different propeller disk load on the aerodynamic performance of the three-dimensional tandem wing system. The investigation examined various combinations of pressure rise percentages (Δp) applied across the propeller actuator disks positioned upstream of the fore wing (Fore wing Δp_O), the overlapping region of the hind wing (Hind wing Δp_O), and the non-overlapping wingtip region of the hind wing (Hind wing Δp_{NO}). The injection momentum coefficients for the fore wing and hind wing were maintained at $C_{\mu,f} = 1.0$ and $C_{\mu,r} = 4.0$, respectively, based on the optimal values identified in the 2D analysis. Table 4 summarizes the aerodynamic performance parameters for the trade study of ten configurations, presenting the total system lift coefficient ($C_{L,t}$), drag coefficient ($C_{D,t}$), and power coefficient (P_{ct}). The subscripts t indicates total system values normalized by the combined planform area of both wings as expressed in Eq. (11) to (19). The trade study varies the Δp_O for the fore wing and hind wing overlapped part, and the outer part of the hind wing without overlapping. The design goal is to have the $C_{L,t}$ of 55 with the resultant force angle ϵ between -85° and 85°. The jet momentum coefficient is held constant for both wings.

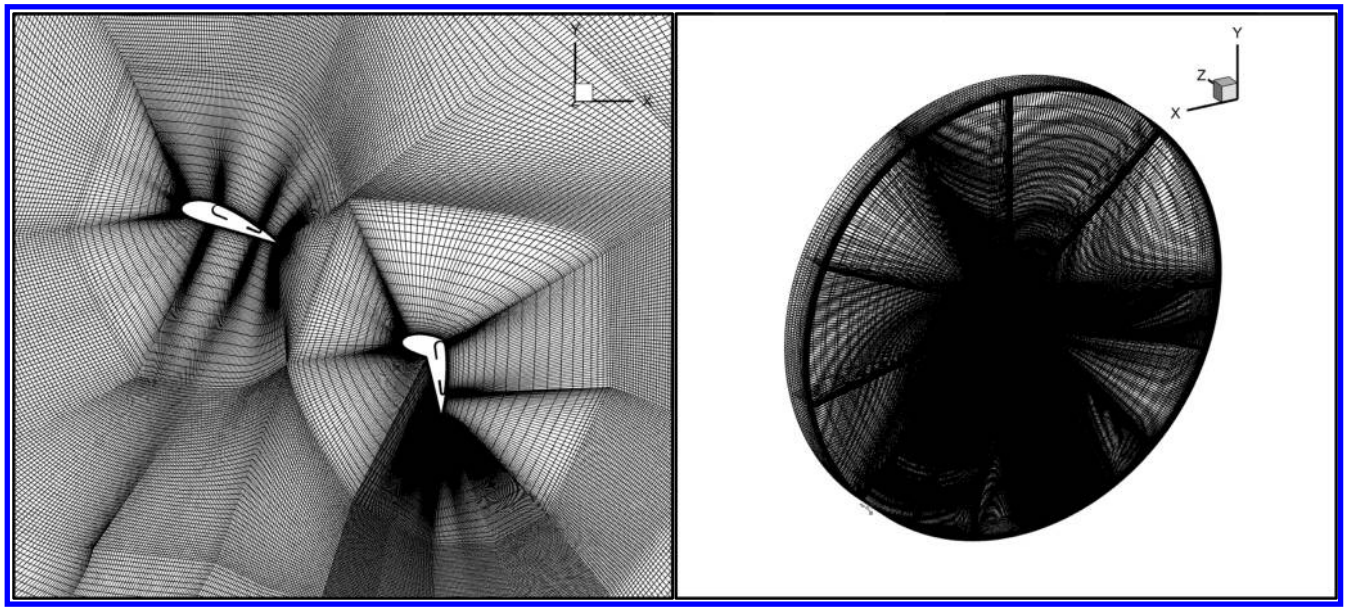

Figure 7: 3D mesh topology

Table 4: Results for 3D

Case	Part	AR	β	Δp_O	Δp_{NO}	C_μ	C_L	C_D	P_c	Γ	Flow attachment	ϵ
Case 1	Fore wing	6.66	0	2.4		1	-1.27	-19.32	6.53	1.13	A	
	Hind wing	20	60	2.4	2.4	4	33.65	49.79	38.21	1.44	A / A	
	Propeller						13.45	-36.96	65.93			
	Total						38.38	-4.45	96.22			-83.39
Case 2	Fore wing	6.66	0	2.7		1	-0.40	-18.83	6.56	1.13	A	
	Hind wing	20	60	2.7	2.7	4	36.38	52.45	37.92	1.44	S / A	
	Propeller						15.12	-41.55	78.57			
	Total						42.31	-6.92	108.65			-80.72
Case 3	Fore wing	6.66	0	3.0		1	0.30	-18.72	6.53	1.13	A	
	Hind wing	20	60	3.0	3.0	4	35.03	51.89	38.21	1.47	S / A	
	Propeller						16.79	-46.13	91.94			
	Total						43.14	-11.89	122.23			-74.59
Case 4	Fore wing	6.66	0	3.5		1	1.03	-18.22	6.36	1.13	A	
	Hind wing	20	60	3.5	3.5	4	37.97	56.67	40.79	1.47	S / A	
	Propeller						19.57	-53.77	115.67			
	Total						48.31	-15.82	147.85			-71.87
Case 5	Fore wing	6.66	0	2.7		1	-0.21	-18.93	6.59	1.13	A	
	Hind wing	20	60	3.5	3.5	4	38.74	56.92	40.58	1.47	S / A	
	Propeller						18.58	-51.05	107.03			
	Total						47.59	-13.10	139.11			-74.61
Case 6	Fore wing	6.66	0	2.7		1	-0.31	-18.92	6.55	1.13	A	
	Hind wing	20	60	4.0	4.0	4	41.44	60.57	40.81	1.47	S / A	
	Propeller						20.75	-57.00	126.27			
	Total						51.75	-16.31	158.51			-72.51
Case 7	Fore wing	6.66	0	2.2		1	-1.15	-19.23	6.74	1.13	A	
	Hind wing	20	60	2.2	4.0	4	42.95	61.65	36.93	1.43	A / A	
	Propeller						17.52	-48.14	98.00			
	Total						49.45	-6.71	127.39			-82.27
Case 8	Fore wing	6.66	0	2.7		1	-0.20	-18.77	6.49	1.13	A	
	Hind wing	20	60	2.2	4.0	4	43.71	62.12	37.00	1.43	A / A	
	Propeller						18.13	-49.82	103.18			
	Total						50.87	-7.93	132.56			-81.14
Case 9	Fore wing	6.66	0	2.2		1	-1.22	-19.21	6.67	1.13	A	
	Hind wing	20	60	2.7	4.0	4	44.39	63.00	36.78	1.43	A / A	
	Propeller						18.25	-50.15	104.21			
	Total						51.24	-7.71	133.47			-81.45
Case 10	Fore wing	6.66	0	2.2		1	-0.76	-19.17	6.63	1.13	A	
	Hind wing	20	60	2.7	4.5	4	47.15	65.71	38.31	1.45	A / A	
	Propeller						19.69	-54.09	116.72			
	Total						54.86	-9.34	146.45			-80.34

* Δp_O: Δp at the overlapping region. Δp_{NO}: Δp at the non-overlapping region.

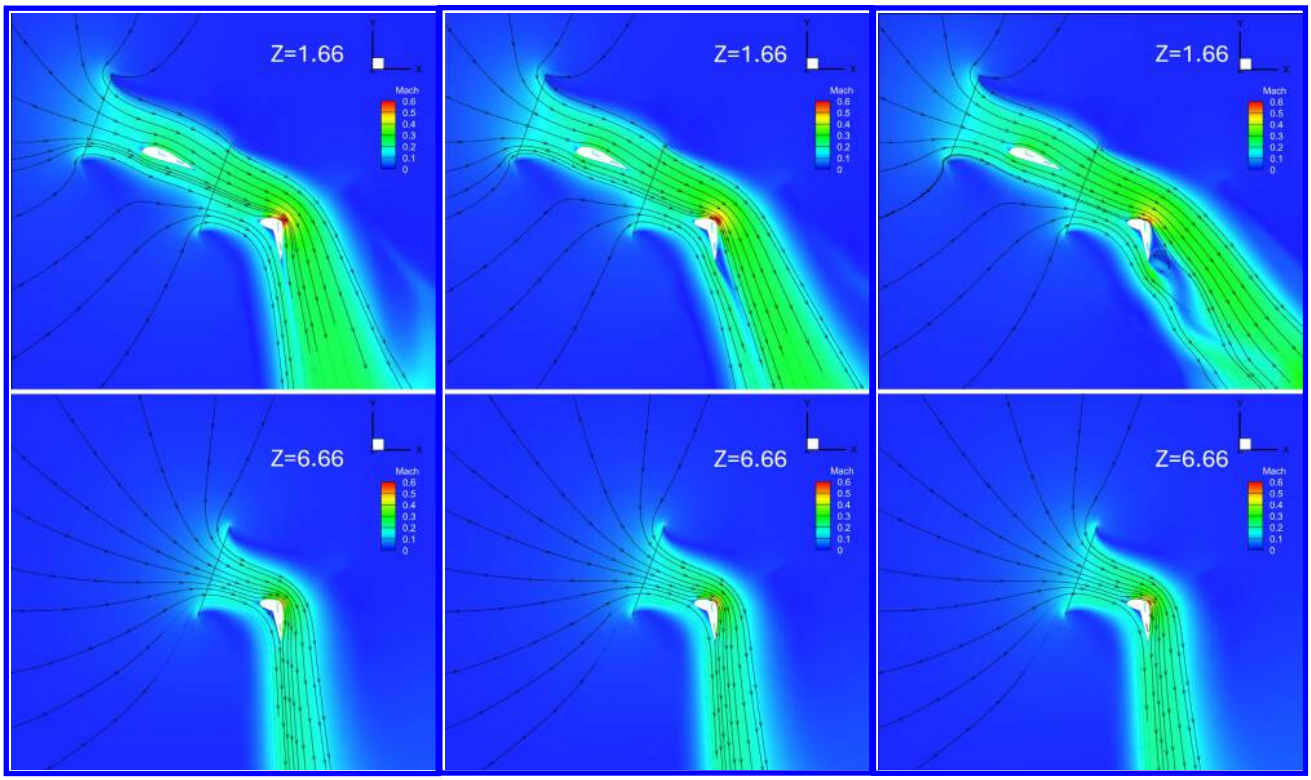

Figure 8: Mach of case 1 (F:Δp_O=2.4%, H:Δp_O=2.4%,Δp_{NO}=2.4%)

Figure 9: Mach of case 2 (F:Δp_O=2.7%, H:Δp_O=2.7%,Δp_{NO}=2.7%)

Figure 10: Mach of case 3 (F:Δp_O=3.0%, H:Δp_O=3.0%,Δp_{NO}=3.0%)

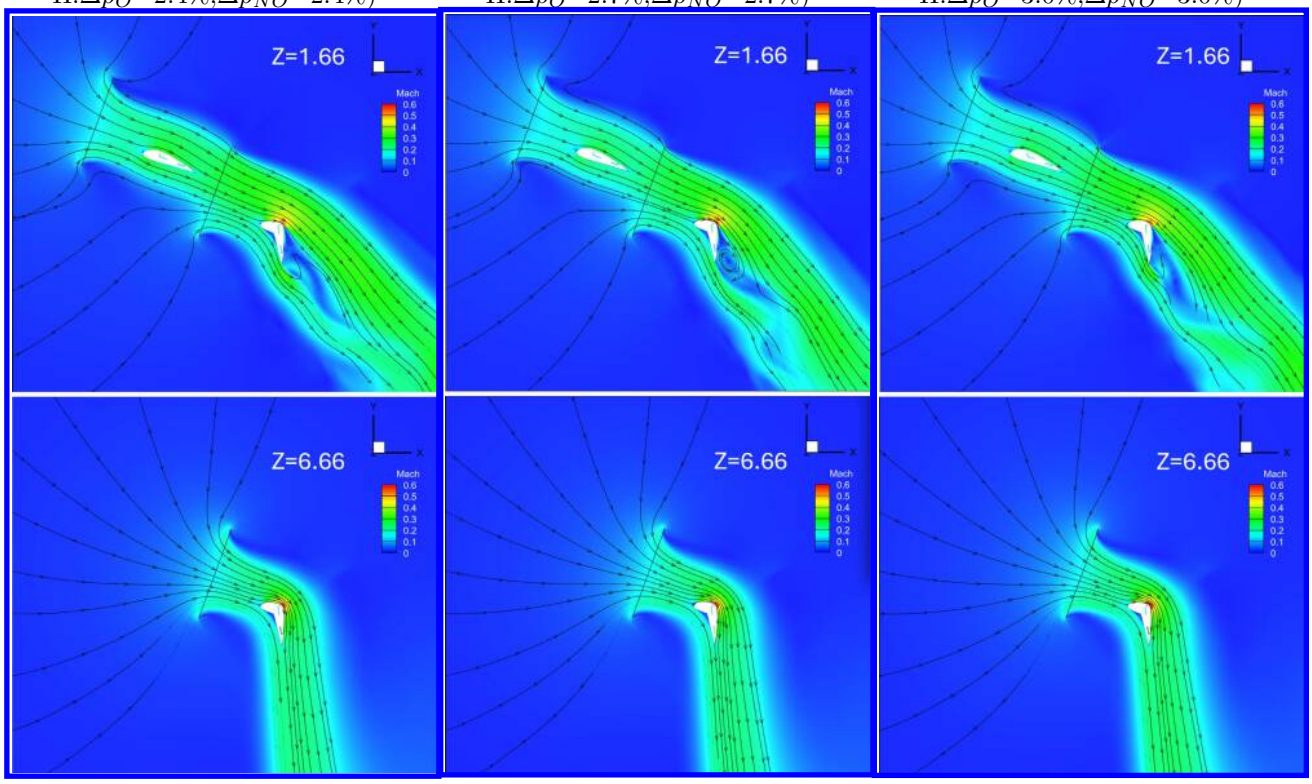

Figure 11: Mach of case 4 (F:Δp_O=3.5%, H:Δp_O=3.5%,Δp_{NO}=3.5%)

Figure 12: Mach of case 5 (F:Δp_O=2.7%, H:Δp_O=3.5%,Δp_{NO}=3.5%)

Figure 13: Mach of case 6 (F:Δp_O=2.7%, H:Δp_O=4.0%,Δp_{NO}=4.0%)

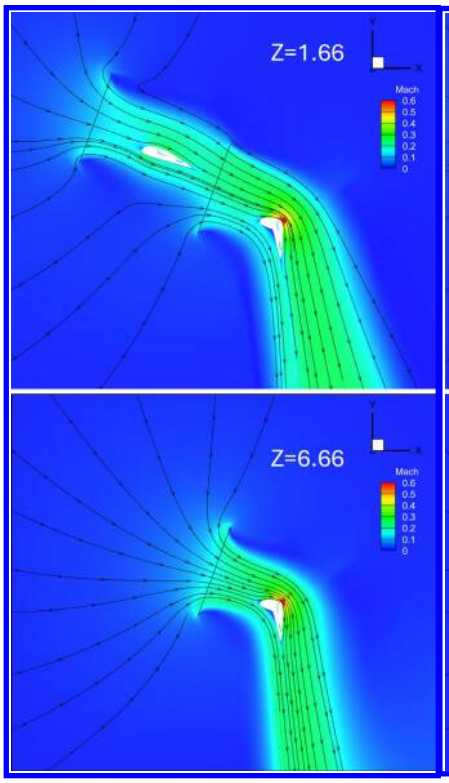

Figure 14: Mach of case 7 (F:Δp_O=2.2%, H:Δp_O=2.2%,Δp_{NO}=4.0%)

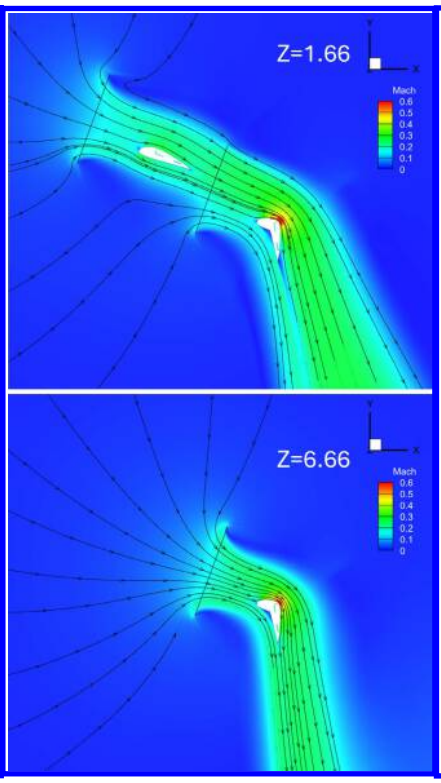

Figure 15: Mach of case 8 (F:Δp_O=2.7%, H:Δp_O=2.2%,Δp_{NO}=4.0%)

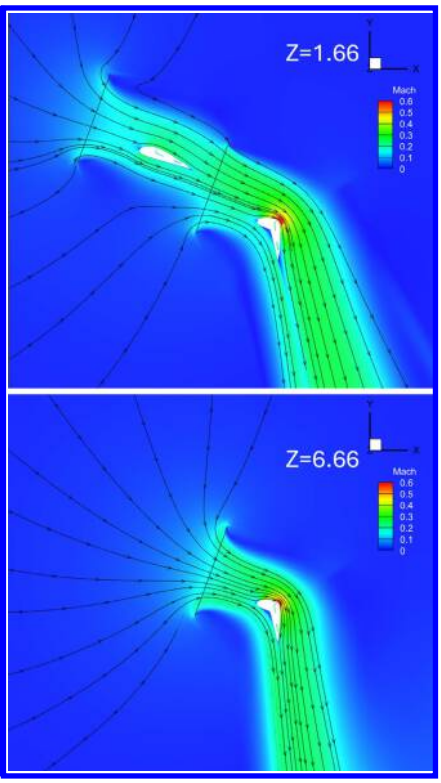

Figure 16: Mach of case 9 (F:Δp_O=2.2%, H:Δp_O=2.7%,Δp_{NO}=4.0%)

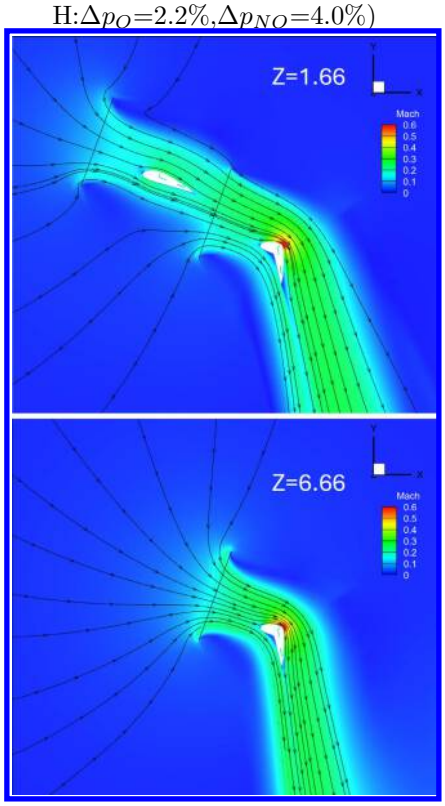

Figure 17: Mach of case 10 (F:Δp_O=2.2%, H:Δp_O=2.7%,Δp_{NO}=4.5%)

The results reveal significant insights into the flow physics and performance limitations of the tandem wing system. All the cases have the same momentum coefficient C_μ of 1 for the fore wing and 4 for the hind wing to minimize the CFJ power coefficient for the targeted total C_L of 55. Cases 2 through 6 show flow detachment on the overlapping hind wing, indicating that when the summation of the Δp of the fore and hind wing in the overlapping part is too high (e.g.,$\Delta p > 4.9$), the jet momentum C_μ on the hind wing is insufficient to turn the flow. The flow sucked by the fore wing's Δp adds to the flow entering the hind wing's propeller, which results in insufficient energy for the hind wing's coflow jet to attach the flow at the same C_μ. In Case 2, the sum of the fore and hind wing Δp is 5.4, which is larger than the sum of 4.4 to 4.9 in Case 1 and Cases 7 through 10, leading to the onset of separation on the hind wing. Cases 3 through 6 have a Δp sum of 6 to 7, and significant separation on the hind wing can be observed from the flow field in Fig. 8 - Fig. 17.

Case 6 and Case 8 share identical conditions with the exception of the hind wing Δp, where Case 6 has a value of 4.0 %, which is nearly double that of Case 8. Although Δp is increased in Case 6, the overall C_L remains similar at a level of 51 due to the occurrence of flow separation. Additionally, the thrust of case 6 becomes stronger due to the propeller's force, resulting in worse outcomes for both the resultant force and ϵ.

Case 8 and Case 9 have opposite Δp conditions for the fore wing and hind wing in the overlapping part, and both show well-attached flow and similar overall performance. However, when the Δp of the hind wing is larger, the flow pulled by the hind wing's propeller is larger, resulting in a lower C_L for the fore wing and a higher C_L for the hind wing. Since this characteristic can affect the pitching moment, further study is necessary.

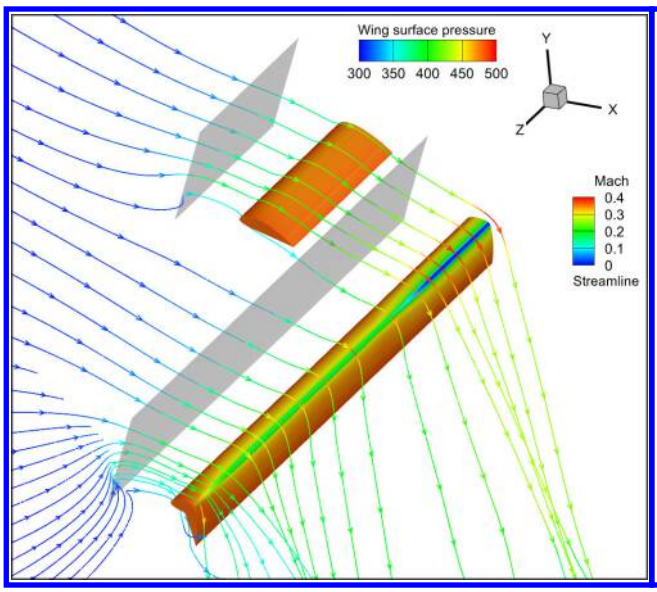

Figure 18: Flow field of case 1 (F:Δp_O=2.4%, H:Δp_O=2.4%,Δp_{NO}=2.4%)

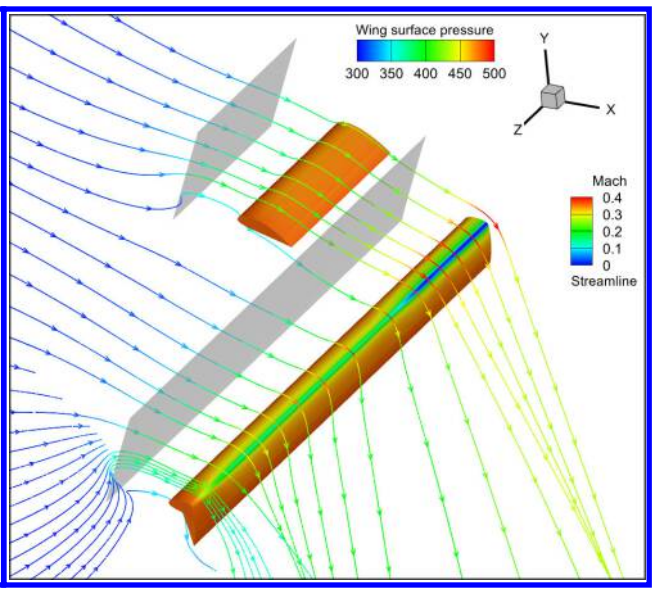

Figure 19: Flow field of case 2 (F:Δp_O=2.7%, H:Δp_O=2.7%,Δp_{NO}=2.7%)

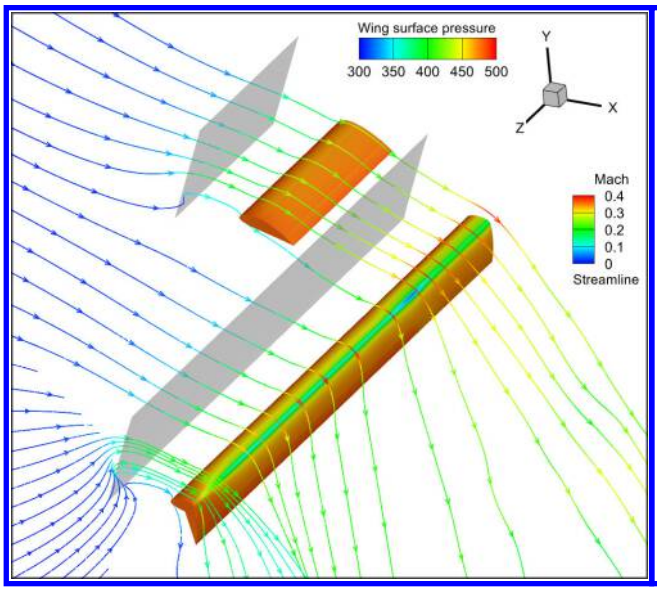

Figure 20: Flow field of case 3 (F:Δp_O=3.0%, H:Δp_O=3.0%,Δp_{NO}=3.0%)

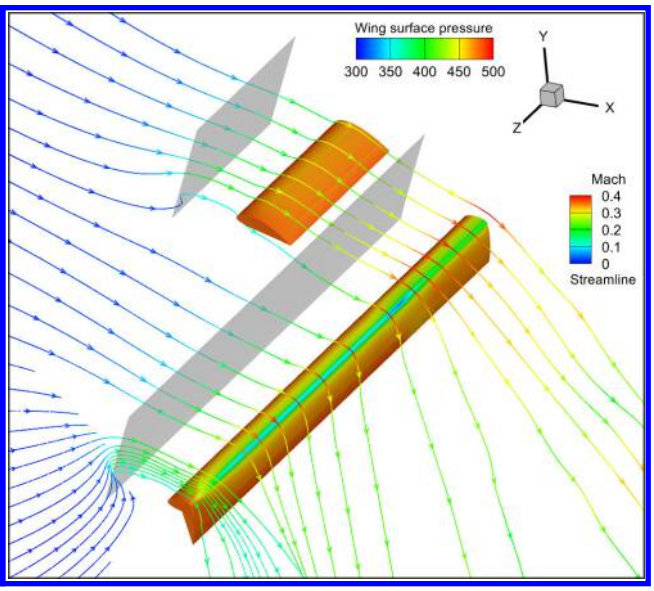

Figure 21: Flow field of case 4 (F:Δp_O=3.5%, H:Δp_O=3.5%,Δp_{NO}=3.5%)

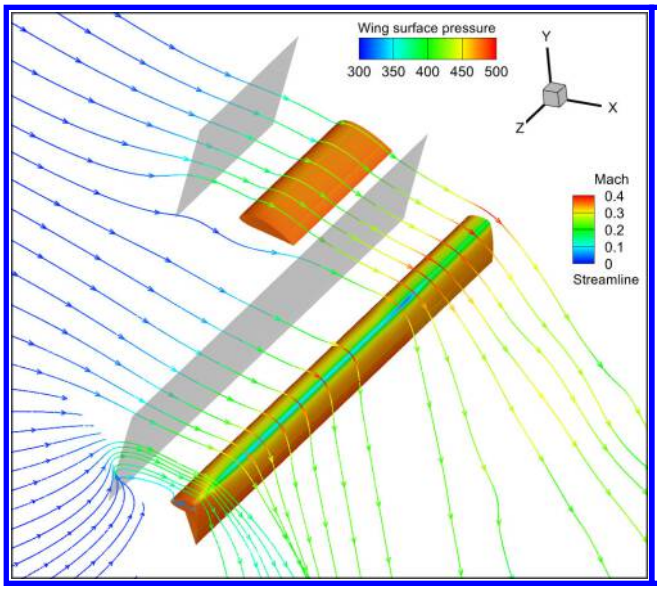

Figure 22: Flow field of case 5 (F:Δp_O=2.7%, H:Δp_O=3.5%,Δp_{NO}=3.5%)

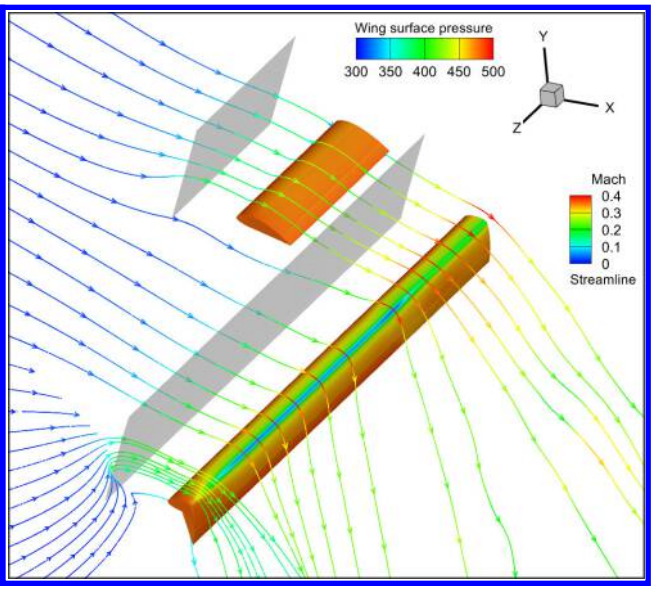

Figure 23: Flow field of case 6 (F:Δp_O=2.7%, H:Δp_O=4.0%,Δp_{NO}=4.0%)

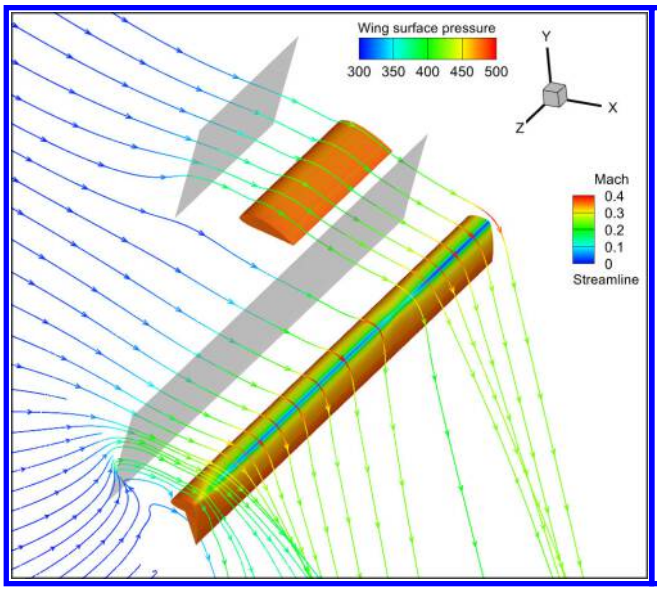

Figure 24: Flow field of case 7 (F:Δp_O=2.2%, H:Δp_O=2.2%,Δp_{NO}=4.0%)

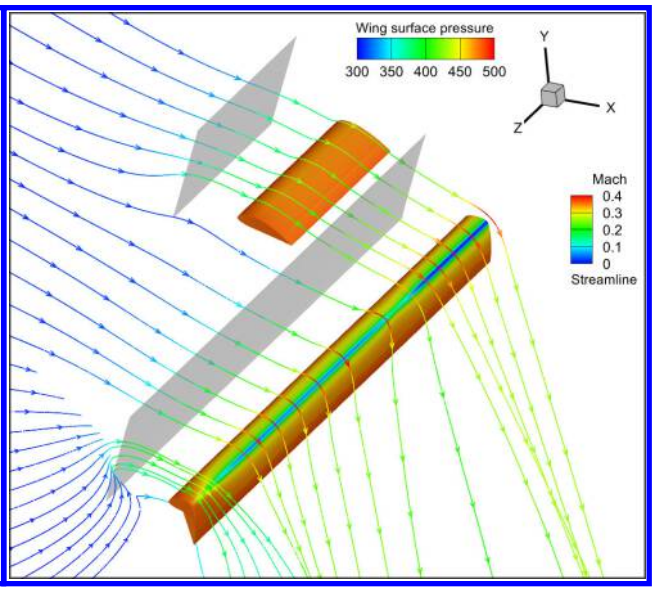

Figure 25: Flow field of case 8 (F:Δp_O=2.7%, H:Δp_O=2.2%,Δp_{NO}=4.0%)

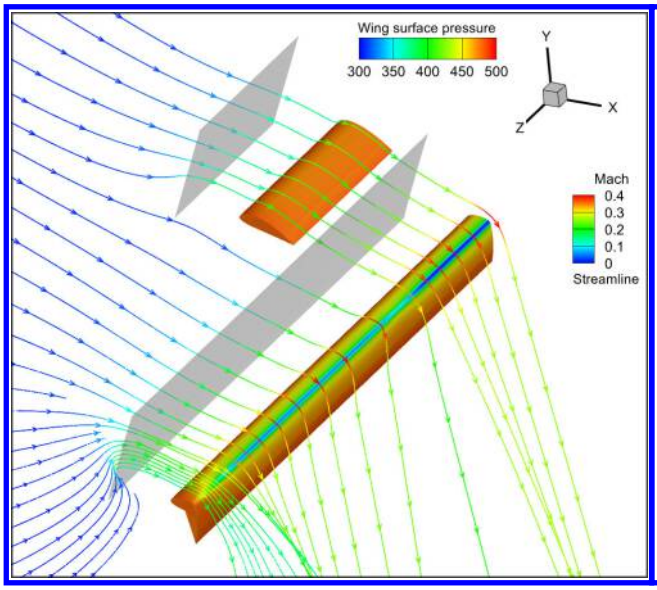

Figure 26: Flow field of case 9 (F:Δp_O=2.2%, H:Δp_O=2.7%,Δp_{NO}=4.0%)

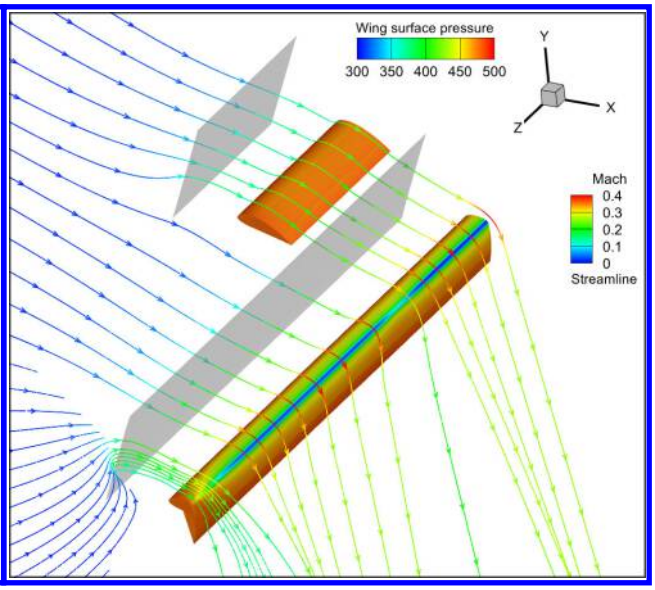

Figure 27: Flow field of case 10 (F:Δp_O=2.2%, H:Δp_O=2.7%,Δp_{NO}=4.5%)

Fig. 18 - Fig. 27 shows the 3D flow field of the tandem wing system with the surface colored by the pressure contours and the streamlines colored by the Mach number. It shows that the flow from farfield has very low speed as the flow is at static condition. The flow is accelerated and energized by the propellers. At the shoulder of the flap, the pressure is the lowest as the suction peak of the flapped wing. The inner span overlapping part of the hind wing has higher lift load than the outer span part due to the overall higher propeller disk load of the two propellers. The flow is deflected well by the hind wing so that the system generates the required total lift as shown in Table 4. Fig. 20 - Fig. 23 shows the overall flow field of Case 3 through Case 6, where separation occurs on the overlapping hind wing. On the other hand, Fig. 27 shows that the flow is well attached overall. for Case 10, which represents the

optimal configuration among those studied, achieving a total system lift coefficient of approximately 55. These results demonstrate that the tandem FCFJ configuration with deflected slipstream can generate sufficient lift force for vertical takeoff and landing.

However, the overall lift and direction design require an iteration of the disk load of the front and rear propeller, the injection momentum coefficient of each wing, and the distribution of the disk load of the hind wing. A systematic optimization could be beneficial. To further improve the system's power efficiency, future work needs to include the following tasks: 1) Trim the aircraft with pitching static stability, which would need to iterate lift distribution between the fore and hind wings. 2) Control the resultant force to be near 90° at hover. 3) Achieve smooth transition from hover to cruise by controlling the CFJ flap, propeller disk strengths, and CFJ strengths.

6 Conclusions

When the tandem airfoils are close in the streamwise direction, the numerical simulation indicates that when both airfoil has the flap deflected at 60 degrees ,the hind airfoil has severely separated flow with very low lift coefficient because the freestream flow is mostly pulled and deflected by the fore airfoil. A feasible configuration employs the fore airfoil without deflection ($\beta = 0$) to accelerate and energize the oncoming flow, while the hind airfoil operates with large deflection angle ($\beta = 60$ degrees) to achieve effective slipstream deflection. This asymmetric deflection strategy enables the system to generate required hover lift coefficients while substantially reducing both CFJ power consumption and propeller disk load compared to single airfoil configurations with equivalent total lift. The optimal 2D configurations with stagger distance $S_t = 2.5C$ and vertical gaps $G = 0$ and $G = -0.5C$ demonstrated approximately 67-70% reduction in total power consumption relative to the non-tilted single baseline airfoil while maintaining flow attachment with $C_\mu = 5$ [22].

The three-dimensional simulations apply these findings to practical finite aspect ratio wings, investigating the effects of different propeller disk loads across the wing span. The computational study examined ten configurations with varying pressure rise distributions (Δp) applied to the fore wing, overlapping hind wing region, and non-overlapping hind wing outer span region.

The optimal configuration (Case 10) achieves a total lift coefficient of approximately 55, validating the feasibility of the tandem FCFJ concept for Martian VTOL operations. This research establishes the aerodynamic feasibility of tandem FCFJ configurations for VTOL hover operations in the thin Martian atmosphere without requiring complex mechanical systems for rotor or wing tilting. Future work will focus on further optimization of geometric parameters including stagger distance, vertical gap, and individual airfoil deflection angles, as well as detailed analysis of CFJ momentum coefficient requirements for each airfoil element. Integration of propeller performance models beyond the actuator disk approximation and investigation of transition flight regimes between hover and forward cruise will provide comprehensive design guidelines for Mars VTOL aircraft employing this innovative configuration.

7 Acknowledgment

The authors would like to acknowledge the computing resources provided by the Coflow Jet, LLC. The teaching assistantship support from the University of Miami is also acknowledged.

Disclosure: The University of Miami and Dr. Gecheng Zha may receive royalties for future commercialization of the intellectual property used in this study. The University of Miami is also equity owner in CoFlow Jet, LLC, licensee of the intellectual property used in this study.

References

[1] G. Zha, Y. Ren, M. Anhalzer, M. A. Mischna, and M. M. Sori, "Mars Aerial and Ground Global Intelligent Explorer (MAGGIE): Mission Feasibility Study," *Proceedings of AIAA SciTech Forum 2026, 12 January 2026 - 16 January 2026, Orlando, FL*, 2026.

[2] Y. Ren and G. Zha, "Design and Analysis of Tandem Wing Aircraft at Ultra-Low Reynolds Numbers in Cruise Condition," *AIAA Paper 2025-3639, AIAA AVIATION FORUM AND ASCEND 2025, 21 - 25 July 2025, Las Vegas, Nevada*, 2025.

[3] Yan Ren, Gecheng Zha, "Performance Enhancement by Tandem Wings Interaction of CoFlow Jet Aircraft," *AIAA Paper 2021-1823, AIAA SciTech Forum, 11–15; 19–21 January 2021, VIRTUAL EVENT*, 2021.

[4] Ren, Y. and Zha, Gecheng, "Simulation of 2D CoFlow Jet Deflected Slipstream VTOL Transition Transient Flows," *10th Annual Electric VTOL Symposium, Mesa, AZ, Jan. 24-26*, 2023.

[5] GeCheng Zha, "Feasibility Study of Deflected Slipstream Airfoil for VTOL Hover Enabled by CoFlow Jet," *AIAA Aviation Forum 2023, 12–16 June 2023, San Diego, CA*, 2023.

[6] G. Zha, Y. Ren, and W. Fredericks, "Design and Testing of Deflected Slipstream Airfoil for VTOL Hover Enabled by CoFlow Jet," *AIAA Paper 2024-4420, AIAA AVIATION FORUM AND ASCEND 2024, 29 July - 2 August 2024, Las Vegas, Nevada*, 2024.

[7] Y. Ren and G. Zha, "2D Fluid-Body Interaction Simulation of CoFlow Jet Deflected Slipstream VTOL Transition Flight," *AIAA Paper 2024-4419, AIAA AVIATION FORUM AND ASCEND 2024, 29 July - 2 August 2024, Las Vegas, Nevada*, 2024.

[8] Jaehyoung Jeon, Yan Ren, and Gecheng Zha, "Toward Ultra-High Cruise Lift Coefficient Using Flapped CoFlow Jet Airfoil," *AIAA SciTech Forum, January 23-27*, 2023.

[9] G.-C. Zha, W. Gao, and C. Paxton, "Jet Effects on Co-Flow Jet Airfoil Performance," *AIAA Journal, No. 6,*, vol. 45, pp. 1222–1231, 2007.

[10] K. Xu and G. Zha, "Design of high specific speed mixed flow micro-compressor for co-flow jet actuators," *ASME Paper GT-2019-90980, ASME IGTI Turbo Expo 2019, Phoenix, Arizona, USA, June 17 - 21*, 2019.

[11] Paula A. Barrios, Yan Ren, GeCheng Zha, "Simulation of 3D Co-Flow Jet Airfoil Control with Micro-Compressor Actuator at High Angles of Attack," *AIAA Aviation Forum 2023, 12–16 June 2023, San Diego, CA*, 2023.

[12] P. R. Spalart and S. R. Allmaras, "A one-equation turbulence model for aerodynamic flows," in *30th Aerospace Sciences Meeting and Exhibit, Aerospace Sciences Meetings, Reno, NV, USA, AIAA Paper 92-0439*, 1992.

[13] Y.-Q. Shen and G.-C. Zha, "Large Eddy Simulation Using a New Set of Sixth Order Schemes for Compressible Viscous Terms ," *Journal of Computational Physics*, vol. 229, pp. 8296–8312, 2010.

[14] Zha, G.C., Shen, Y.Q. and Wang, B.Y., "An improved low diffusion E-CUSP upwind scheme ," *Journal of Computer and Fluids*, vol. 48, pp. 214–220, Sep. 2011.

[15] Y.-Q. Shen and G.-Z. Zha , "Generalized finite compact difference scheme for shock/complex flowfield interaction," *Journal of Computational Physics*, vol. doi:10.1016/j.jcp.2011.01.039, 2011.

[16] Shen, Y.-Q. and Zha, G.-C. and Wang, B.-Y., " Improvement of Stability and Accuracy of Implicit WENO Scheme," *AIAA Journal*, vol. 47, No. 2, pp. 331–344, 2009.

[17] Shen, Y.-Q. and Zha, G.-C. and Chen, X.-Y., " High Order Conservative Differencing for Viscous Terms and the Application to Vortex-Induced Vibration Flows," *Journal of Computational Physics*, vol. 228(2), pp. 8283–8300, 2009.

[18] Shen, Y.-Q. and Zha, G.-C. , " Improvement of the WENO Scheme Smoothness Estimator," *International Journal for Numerical Methods in Fluids*, vol. DOI:10.1002/fld.2186, 2009.

[19] G.-C. Zha and E. Bilgen, "Numerical Study of Three-Dimensional Transonic Flows Using Unfactored Upwind-Relaxation Sweeping Algorithm," *Journal of Computational Physics*, vol. 125, pp. 425–433, 1996.

[20] B.-Y. Wang and G.-C. Zha, "A General Sub-Domain Boundary Mapping Procedure For Structured Grid CFD Parallel Computation," *AIAA Journal of Aerospace Computing, Information, and Communication*, vol. 5, No.11, pp. 2084–2091, 2008.

[21] Y.-Q. Shen, G.-C. Zha, and B.-Y. Wang, "Improvement of Stability and Accuracy of Implicit WENO Scheme ," *AIAA Journal*, vol. 47, pp. 331–344, 2009.

[22] Jaehyoung Jeon; Anthony Diaz; Yan Ren; Gecheng Zha, "Study of 2D Hover Performance Using Flapped Coflow Jet airfoil at Low Reynolds Numbers," *AIAA Paper 2025-3703,AIAA Aviation Forum 2025, 21–25 July 2025, Las Vegas, Nevada*, 2025.